Wang, Z. and Li, P. (2017) Voronoi cell finite element modelling of the intergranular fracture mechanism in polycrystalline alumina. *Ceramics International*, 43(9), pp. 6967-6975. (doi:10.1016/j.ceramint.2017.02.121)

This is the author's final accepted version.

There may be differences between this version and the published version. You are advised to consult the publisher's version if you wish to cite from it.

http://eprints.gla.ac.uk/145534/

Deposited on: 14 August 2017

Voronoi cell finite element modelling of the intergranular fracture mechanism in polycrystalline alumina

Zhiyong Wang [a], Peifeng Li [a,b,*]

[a] School of Mechanical and Aerospace Engineering, Nanyang Technological University, Singapore

[b] School of Engineering, University of Glasgow, Glasgow, UK

[*] Corresponding author's email: peifeng.li@ntu.edu.sg and peifeng.li@glasgow.ac.uk (P. Li);

Tel: +65 6790 4766.

Abstract

The mechanisms of fracture in polycrystalline alumina were investigated at the grain level using both the micromechanical tests and finite element (FE) model. First, the bending experiments were performed on the alumina microcantilever beams with a controlled displacement rate of 10 nm s^{-1} at the free end; it was observed that the intergranular fracture dominates the failure process. The full scale 3D Voronoi cell FE model of the microcantilever bending tests was then developed and experimentally validated to provide the insight into the cracking mechanisms in the intergranular fracture. It was found that the crystalline morphology and orientation of grains have a significant impact on the localised stress in polycrystalline alumina. The interaction of adjacent grains as well as their different orientations determines the localised tensile and shear stress state in grain boundaries. In the intergranular fracture process, the crack formation and propagation are predominantly governed by tensile opening (mode I) and shear sliding (mode II) along grain boundaries. Additionally, the parametric FE predictions reveal that the bulk failure load of the alumina microcantilever increases with the cohesive strength and total fracture energy of grain boundaries.

Keywords: Fracture; Micromechanics; Ceramics; Voronoi tessellation; Finite element model.

1   Introduction

The mechanical behaviour of ceramic materials is intrinsically determined by the microstructural feature. For example, the size, morphology and orientation of individual grains can affect the localised stress distribution and thus the bulk behaviour. To enable the design and use of ceramics in various industrial applications, there is a necessity to understand the underlying mechanisms for deformation and failure process in microscopic scale [1, 2].

Microstructural heterogeneities and anisotropic nature of grains have the remarkable impact on the failure of ceramics. In polycrystalline ceramics such as alpha alumina, the crack incident angle and the ratio of the grain boundary fracture energy to the surface energy of crystal planes affect the modes of crack propagation: either along grain boundaries (intergranular fracture) or through individual grains (transgranular fracture) [3-5]. Kraft et al. reported the pronounced influence of the grain boundary distribution upon the percentage of transgranular fracture in polycrystalline alumina subjected to tensile loads [3]. The chemical additive can change the fracture modes; the intergranular fracture dominates in aluminium nitride with 2 wt% CaO additives whilst transgranular fracture in the undoped ceramic [6]. Moreover, the fracture mechanism in ceramics is sensitive to strain rates [7-10]. At the low rate, the subcritical crack nucleation and growth are suppressed as a result of the crack kinetics; thus cracks propagate along grain boundaries. At the high rate, the instantaneous release of strain energy near the crack tip leads to the crack propagation through the individual grain. It has been reported that the intergranular fracture is the

governing failure mode of the polycrystalline alumina subjected to quasi-static compression, while a combined intergranular and transgranular fracture mode dominates under dynamic compression at the strain rate above a critical value [9-11]. Although the elastic deformation of alumina ceramics is insensitive to grain sizes, the transverse bending strength varies with the grain size over a wide range of temperatures; in addition the transgranular instead of intergranular fracture tends to occur with the increase of temperature up to 1500 °C [12, 13]. It is experimentally difficult to directly probe the rapid crack propagation process in brittle ceramics even at the low loading rate. Nonetheless, the numerical simulation at the grain level can offer the insight into the fracture mechanism in polycrystalline ceramics.

Micromechanical finite element (FE) modelling [5, 14-19] and molecular dynamics simulation [20] have been the prevalent numerical techniques to study the intergranular and transgranular crack propagation behaviour in polycrystalline materials. However, the molecular dynamics approach simulates the material behaviour in the nanoscale and consequently requires substantial computational time for microscopic fracture domain consisting of grains (e.g., grain size 1 to 10 μm) [20]. A large amount of research has focused on FE modelling to explore the localised stress distribution and micromechanical fracture behaviour (such as tensile cracking) of ductile metals and brittle ceramics with heterogeneous microstructure [14-19]. However, the limitations exist in these available FE models [14-19]: interfacial properties between grains were neglected [14-16], pre-cracks were introduced in grains [17, 18] and regular instead of random grain distribution was assumed [19]. A

micromechanical FE model to simulate the crack initiation and propagation of polycrystalline ceramics needs to consider the anisotropic properties of individual grains, interfacial behaviour of grain boundaries, and real heterogeneous microstructure.

In the micromechanical FE simulation, the cohesive layer model has been widely accepted to track the intergranular fracture process, whilst the failure criterion for single grains can be specified for the transgranular fracture. The constitutive response of the cohesive layer defines the interfacial behaviour between grains and thus enables the prediction of the crack initiation and propagation at the grain level. The cohesive layer model has been employed to investigate the 2D crack growth in isotropic solids [3, 21, 22]. However, a more realistic and accurate numerical simulation also requires the 3D representation of the grains and grain boundaries.

The grains in a polycrystalline material can be reconstructed based on the real heterogeneous microstructure directly examined in experiments or using an idealised representative elementary volume (REV). The crystallographic feature of the grains can be characterised using the destructive (e.g., the combined focused ion beam (FIB) micromachining and electron backscatter diffraction [23, 24]) or non-destructive (e.g., 3D x-ray diffraction [25]) experimental techniques. However, it is challenging to apply these experimental techniques to extract the crystallographic information of hard and brittle polycrystalline ceramics due to the considerable micromachining time (destructive) and the relatively low spatial resolution (non-destructive). To represent a polycrystalline ceramic, the virtual idealised grains can be created with either the

regular morphology or the analytical random morphology. It is easy to generate and mesh a REV microstructure with the regular crystalline morphology [26]. Voronoi tessellation is one of the established methods to generate the analytical random morphology of a REV polycrystalline microstructure in which the grains are defined with straight edges and curved/planar faces [18, 27-30]. The idealised REV microstructure modelled by Voronoi tessellation has been widely accepted as the first order approximation of polycrystalline materials to investigate their behaviour [5, 31].

The aim of this study was to investigate the underlying mechanisms of the fracture behaviour in polycrystalline alumina subjected to low strain rate loads. The bending experiments on the alumina microcantilever beams were conducted to probe the deformation and the fracture mode at the grain level. A full scale 3D Voronoi cell FE model of the microcantilever bending test was developed to simulate the localised stress distribution/evolution and to track the crack initiation and propagation in the alumina. The FE predictions were analysed to reveal the mechanisms of crack propagation during the fracture process. The FE model of the alumina microcantilever beam was rerun as a function of the interfacial grain boundary property to explore its impact on the intergranular fracture behaviour.

2 Experimental procedure and observations

2.1 Materials and microstructure

The alumina specimens of the purity 99.5% (Chair Man Hi-Tech Co. Ltd., Taiwan) were polished and then thermally etched (annealing in the air atmosphere at

1200 °C). Fig. 1 shows the representative polycrystalline microstructure of alumina observed in the scanning electron microscope (SEM). Further analysis reveals that the average grain size is approximately 1.2 μm.

2.2 *Microcantilever bending experiments*

The alumina microcantilever beams were prepared on a polished alumina specimen in an FEI Helios Nanolab 450S (FEI Co., OR, USA) using the focused ion beam micromachining technique. A gallium ion beam operating at 30 kV and 10 nA was applied to cut the microcantilever beam specimens (Fig. 2). The microcantilever beam was approximately 20 μm in length. The transverse cross section was an equilateral triangle with the side length 5 μm. Note that it is difficult to prepare other types of cross sections such as a rectangle using the FIB technique, because the sample stage can only be tilted to a limited angle.

Microcantilever bending experiments were conducted in an MTS Nanoindenter XP (MTS Systems Corp., MN, USA). The Berkovich indenter was applied to the top surface near the free end of the microcantilever beam at a controlled displacement rate 10 nm s^{-1} until the beam failed (Fig. 2). The displacement of the nanoindenter tip as well as the reaction force was recorded during the bending experiments. The final fracture feature in the alumina was examined in the SEM.

2.3   Observations on deformation and intergranular fracture in alumina

Fig. 3(a) shows the typical history of the load (P) applied near the free end of the microcantilever beams. At the initial stage of the bending load, the indentation depth into the alumina surface can be a considerable portion of the total displacement of the nanoindenter tip; thus the load varies nonlinearly with the measured displacement (Fig. 3(b)). Under further loads, the increased deflection of the microcantilever beam (ΔL) dominates the total displacement of the tip. Therefore, the applied load increases approximately linearly with the measured displacement (Fig. 3(b)), representing the elastic deformation of the beam. To characterise the deflection of the microcantilever beam, the measured load versus displacement curve is shifted such that the linear portion passes the origin (Fig. 3(b)). The elastic modulus ($E \approx 390$ GPa) of the bulk alumina can be quantified based on the slope of the curve ($P/\Delta L$):

$$E = \frac{P}{\Delta L} \cdot \frac{L_{\mathrm{A}}^{3}}{3I} \tag{1}$$

where L_{A} is the distance between the nanoindenter tip and the fixed end of the microcantilever, and I is the moment of inertia of the transverse cross section. This measured elastic modulus is slightly lower than the typical modulus of engineering alumina (398–400 GPa for the purity 99.5% [32, 33]), probably due to the small porosity variation (<1%).

The alumina microcantilever beam fails when the measured load reaches the peak (~1.158 mN) and subsequently drops abruptly in the bending experiment (Fig. 3). The SEM examination reveals that the fracture of alumina occurs near the fixed end

of the microcantilever where the internal bending moment is the maximum (see Fig. 4). The fracture surface is uneven and full of sharp edges, implying that the intergranular fracture dictates the failure process of the alumina in the bending test at the displacement rate 10 nm s^{-1}. The previous work by the authors also revealed that under quasi-static uniaxial compression the intergranular fracture is the dominant failure mode in alumina, which is induced by the localised tensile stress [9]. Note that in Fig. 4 a pore is observed in the alumina material despite its high purity of 99.5%. The porosity is <1% according to the manufacturer. The presence of pores may affect the localised stress. The surface of each microcantilever beam was examined prior to the bending experiments so that only the beams with no surface defects were tested.

3 Finite element modelling

A full scale 3D Voronoi cell finite element model of the polycrystalline alumina microcantilever beam was developed in the ABAQUS/Explicit software (Dassault Systèmes Simulia Corp., RI, USA) to simulate the localised stress evolution and fracture process of the beam subjected to quasi-static bending loads (Fig. 5). The FE simulation was rerun with six different sets of random crystalline orientations which were assigned to the grains in the beam. This section describes in details the geometrical generation of the polycrystalline microstructure using Voronoi tessellation, and the constitutive formulation for the individual grains and grain boundaries.

3.1 Voronoi tessellation and FE meshes of polycrystalline alumina

The grains in the 3D domain of polycrystalline alumina microcantilever beam were generated using the hardcore Voronoi tessellation technique in the open source software NEPER [34] (refer to Fig. 5(a)). The number of grains (N) in the domain was estimated in terms of the average grain size as experimentally measured (1.2 μm in Fig. 1) and the volume of the domain. The N nuclei (seeds) were then randomly distributed in the beam domain (i.e., seeding domain). The hardcore Voronoi regulation further specified a minimum repulsion distance (ρ) between any two nuclei (P_i and P_j) as follows.

$$\left| P_i - P_j \right| > \rho \quad \forall i, j = 1,2,...N : i \neq j \tag{2}$$

It can be assumed that: (1) all the nuclei remain in the fixed position and grow simultaneously in all directions at a constant rate, (2) a grain boundary is generated where the grains meet, and (3) there are no voids or overlaps in the Voronoi cells. All the points R_{Pi} in the ith Voronoi cell are closer to the associated nucleus P_i than any other nuclei P_j in the microcantilever beam domain:

$$\left\{ R_{Pi} \right\} = \left\{ x \in X \mid d(P_i, x) \leq d(P_j, x), \ j = 1,2,...N : i \neq j \right\} \tag{3}$$

where P is the nucleus distribution, x is any point in the seeding domain X, and d is the distance. Compared to other regulation methods (e.g., Poisson's), the hardcore Voronoi tessellation can better regularise the cells (grains); and it can qualitatively simulate the first order properties of polycrystalline materials [18].

The Voronoi cells in the microcantilever beam were meshed with tetrahedral FE elements (Fig. 5(b)) using the bottom-up algorithm in the open source meshing software GMSH [35]. The discretisation was performed on the tessellation vertices (0D), edges (1D), faces (2D) and cells (3D) in sequence. The n–D (n = 1, 2, 3) meshes were generated based on the (n-1)–D meshes.

3.2   Anisotropic elastic properties of individual alumina grains

The constitutive behaviour of individual grains in the polycrystalline alumina (alpha alumina in this study) was quantified by the linear anisotropic elastic formulation:

$$\sigma_{ij} = C_{ijkl}\,\varepsilon_{kl} \tag{4}$$

where σ_{ij} and ε_{kl} are the stress and strain tensors, respectively, and C_{ijkl} is the stiffness (elasticity) tensor. Owing to the trigonal crystallographic structure, only six independent elastic constants are required to describe the stiffness matrix C in the stress–strain relation of alumina grains as follows [36].

$$
\begin{bmatrix} \sigma_1 \\ \sigma_2 \\ \sigma_3 \\ \sigma_4 \\ \sigma_5 \\ \sigma_6 \end{bmatrix} =
\begin{bmatrix}
C_{11} & C_{12} & C_{13} & C_{14} & 0 & 0 \\
C_{12} & C_{11} & C_{13} & -C_{14} & 0 & 0 \\
C_{13} & C_{13} & C_{33} & 0 & 0 & 0 \\
C_{14} & -C_{14} & 0 & C_{44} & 0 & 0 \\
0 & 0 & 0 & 0 & C_{44} & C_{14} \\
0 & 0 & 0 & 0 & C_{14} & 0.5\cdot(C_{11}-C_{12})
\end{bmatrix}
\times
\begin{bmatrix} \varepsilon_1 \\ \varepsilon_2 \\ \varepsilon_3 \\ \varepsilon_4 \\ \varepsilon_5 \\ \varepsilon_6 \end{bmatrix} \tag{5}
$$

Numerous studies in the literature [37-39] have reported the consistent elastic constants for alpha alumina. The anisotropic elastic constants used in the present FE models as listed in Table 1 were obtained from the literature [39].

3.3   Cohesive layer for grain boundary

The failure of alumina microcantilever beams is dominated by the intergranular fracture (the failure of the interface between grains) as detailed in Section 2.3. Mechanical properties of the interface (grain boundary) can significantly affect the macroscopic behaviour of alumina. The cohesive layer in ABAQUS was used to model the grain boundary within the alumina. The cohesive elements were produced using the nodes that were shared by any two Voronoi tessellation entities (edges, faces or cells). Fig. 5(c) exhibits the cohesive elements for the grain boundaries in the microcantilever beam.

The constitutive response of cohesive elements was defined by the traction–separation law that assumes the initially linear elastic behaviour followed by the damage initiation and evolution [40-42] (refer to Fig. 6). The linear traction–separation relation (line oa in Fig. 6) defines the elastic behaviour prior to damage. The damage characterised by the stiffness degradation initiates at the separation δ_0 (i.e., traction T_0 at point a, called the cohesive strength). The damage evolves along the line ab until the final fracture occurs at the separation δ_f. The damage evolution process can be quantitatively described by the fracture energy as determined by the area under the traction–separation curve or by the ratio of initial to final separations (δ_0/δ_f).

4 Results and discussion

4.1 Effect of the grain number on bulk elastic behaviour

To validate the representation of grains in the polycrystalline alumina microcantilever beam as in Fig. 5, the effect of the grain number on bulk elastic behaviour was explored through parametric finite element modelling of the cubic representative elementary volume subjected to tension at a strain rate 0.001 s^{-1}. Three cubic REVs were generated to have 30, 60 and 90 grains (average grain size 1.2 μm), respectively (Fig. 7). A total number of 100 simulations were performed for each REV alumina with the specific grain number, using a combination of ten different crystalline morphologies and ten groups of randomly generated grain orientations. The effective Young's modulus representing the bulk elastic behaviour was calculated from the deformation of each cubic REV alumina.

Fig. 8 shows the predicted Young's modulus of the REV alumina as a function of the number of grains. For each grain number, the average modulus as well as the standard deviation was calculated from the 100 FE simulations. The standard deviation is small (<2.5%). As no porosity is assumed in the REV alumina, the predicted average modulus is slightly higher than the typical modulus (398–400 GPa) of engineering alumina with the purity 99.5% and the porosity <1% [32, 33]. The difference of the average Young's modulus among the three grain numbers is negligible (<1%) as shown in Fig. 8. This suggests that the effect of grain number on macroscopic properties of alumina is insignificant if there are at least 2–3 grains in the

characteristic edge. The transverse cross sectional area of the alumina microcantilever beam is similar to the cross sectional area of the cubic REV with 30 grains (Figs. 5 and 7); thus the microcantilever beam can represent a bulk alumina beam. It was reported that for the material with crystals of limited anisotropic elastic properties, an REV composed of more than 20 grains can approximate the bulk material with a small acceptable error (e.g., less than 10%) [28].

4.2   *Validation of FE model on alumina microcantilever beam*

The localised stress evolution as well as the failure and fracture process in the polycrystalline alumina microcantilever beam was simulated in the full-scale FE model with the controlled displacement rate applied at the free end. Fig. 9 shows the predicted load versus displacement curves at the free end of the beam. The six curves are the results of the beam in which all the grains were assigned with six different sets of random crystalline orientations. Based on the six predicted load versus displacement curves (Fig. 9), the bulk elastic modulus as calculated using Eq. (1) is E = 395 GPa with a very small deviation <2%; additionally the load at failure (average 1.207 mN) varies within <3%. Overall, the predicted longitudinal stress (σ_z) is tensile on the top but compressive on the bottom of the microcantilever beam, as shown in Fig. 10. The global stress magnitude is comparable among the simulations using different grain orientations.

The failure and fracture process of the alumina microcantilever was simulated in the FE model (refer to Fig. 11). The prediction exhibits that the intergranular fracture

occurs near the fixed end of the beam as observed in the post-test SEM examinations (compare Figs. 4 and 11). All the six simulations demonstrate the similar failure and fracture process in alumina. The agreement between the FE predictions and the experiments thus validates the developed FE model of the alumina microcantilever beam. However, it should be noted that unlike the microcantilever bending tests by the nanoindenter tip, the initial portion of the predicted curves is almost linear; moreover, the predicted bulk elastic modulus (395 GPa) is slightly greater than the measured modulus (390 GPa). These minor differences from the experiments are attributed to the approximation in the FE model. For example, no indentation is simulated in the model in which the deformation of alumina grains is only elastic.

4.3   Intergranular fracture process in alumina

4.3.1   Localised stress distribution and evolution

The localised longitudinal stress (σ_z) distribution in the grains of the microcantilever beam (Fig. 11) is tracked in one of the FE simulations to investigate the intergranular fracture process in alumina under bending loads. The characteristic lines for grain boundaries are set to be invisible in Fig. 11 in order to better reveal the fracture features in the late stage of loading. Nevertheless, the stress state in each grain can be differentiated due to the anisotropic elastic properties. Fig. 12 demonstrate the evolution of maximum principal stresses in the gain boundaries as well as the crack initiation and propagation during the fracture process. The stresses in both the grains and grain boundaries increase with the applied bending load in the

early stage (refer to Figs. 11(a)–(b) and 12(a)–(b)). After the peak load is reached, the crack initiates and propagates along the grain boundaries (Figs. 11(c)–(e) and 12(c)–(e)), resulting in the intergranular fracture of the alumina. The release of strain energy causes an overall abrupt drop of the load at the free end.

The top portion of the microcantilever beam near the fixed end is subjected to tension whilst the bottom part under compression. The maximum stress occurs on the top and bottom surfaces where the crack is more likely to form. However, the grain orientation (anisotropy of elasticity) causes non-uniform stress distribution at the same distance to the neutral axis. The interaction of the adjacent grains results in the tensile stress concentration in the vicinity of the bottom where grain boundaries meet the bottom edge of the beam, as shown in Fig. 12(b). Therefore, in the present beam with an upside down triangular transverse cross section, the crack tends to initiate from the bottom (refer to Figs. 11(c) and 12(c)) and then propagate along the grain boundaries (Figs. 11(d)–(e) and 12(d)–(e)). However, it should be noted that the crack may initiate from either the top or the bottom near the fixed end, depending on the geometry of the cross section as well as the morphology and orientation of grains.

4.3.2 Mechanisms of intergranular fracture: shear sliding and tensile opening

Both the experiments and FE simulations reveal the intergranular fracture of alumina under the low loading rates. The crystalline morphology and orientation of grains play an important role in the occurrence of localised stresses, which consequently determine the cracking modes during the fracture process: tensile opening (mode I) and shear sliding (mode II). Analysis of the fracture features in the

Voronoi tessellation (Fig. 13(a)) reveals the presence of both the tensile opening and shear sliding modes in the grain boundaries.

Fig. 13(b) further schematically demonstrates the cracking processes in the grains near the fixed end of a microcantilever beam with random grain morphologies and orientations. The applied load at the free end causes the shear force and the maximum bending moment at the fixed end. Microscopically, the interaction of grains as well as the disparity of their orientations determines the actual tensile or shear stress state in the grain boundaries. The formation and propagation of cracks are then dominated by tensile opening or shear sliding. In the intergranular fracture of brittle materials such as alumina, the failure modes in grain boundaries are dictated by the localised stress state which is affected by the external loading condition and the grain morphology and orientation. Note that under uniaxial compression the intergranular fracture in alumina is mainly determined by the localised tensile stress state [9].

4.4   Effect of interfacial grain boundary properties on intergranular fracture

The use of cohesive layers enables modelling of intergranular fracture in alumina subjected to low strain rate loads. The interfacial behaviour (Fig. 6) is quantified by the traction–separation law using parameters such as the initial stiffness, damage initiation (including initial separation δ_0 and cohesive strength T_0) and damage evolution (final separation δ_f). To investigate the effect of cohesive properties on the failure behaviour of alumina ceramics, the FE model of the microcantilever

beam with the same polycrystalline characteristics was rerun as a function of the cohesive strength (T_0 for baseline) and the ratio of initial to final separations ($\delta_0/\delta_f = 1.0$ for baseline). All the FE simulations reveal the similar localised stress state in the beam before the degradation of cohesive layers, thus the same elastic behaviour of the beam. In each simulation, the intergranular fracture process in the beam is observed and dominated by shear sliding and tensile opening modes.

Fig. 14 compares the predicted load versus displacement curves at the free end. Quantitatively, both the load and displacement at failure increase with the cohesive strength and the damage evolution (i.e., the ratio of initial to final separations) of grain boundaries. The variation of the beam behaviour with interfacial grain boundary properties is relatively smaller when the damage initiation ratio δ_0/δ_f is between 0.5 and 1.0. The further reduction of the damage ratio δ_0/δ_f (e.g., between 0.25 and 0.5) suggests the increased total fracture energy of grain boundaries and slow degradation of alumina properties, thus resulting in the increased load at failure of the microcantilever beam (Fig. 14). Considering the brittle failure nature of alumina, the damage initiation ratio δ_0/δ_f was selected to between 0.5 and 1.0 in the present study, as suggested in the literature [42]. In addition, the parametric FE simulation implies that the processing of alumina ceramics can be optimised to improve the grain boundary properties for enhanced fracture toughness.

5   Conclusions

The fracture mechanisms in polycrystalline alumina were investigated using the combined microcantilever bending experiments and the full scale 3D Voronoi cell finite element model. The experimentally validated FE predictions offered the insight into the fracture behaviour at the grain level. The conclusions were drawn as follows.

- Micromechanical bending tests reveal that the intergranular fracture governs the failure process of the polycrystalline alumina subjected to bending loads with a controlled displacement rate 10 nm s^{-1}.

- The crystalline morphology and orientation of grains play an important role in determining the localised stress in alumina. The interaction of adjacent grains as well as the difference of their orientations (anisotropy of elasticity) leads to the non-uniform stress distribution, and in particular, the tensile and shear stress state in grain boundaries.

- The localised stress state dictates the cracking modes during the intergranular fracture. Analysis of the predicted fracture features suggests that the formation and propagation of cracks are dominated by the tensile opening (mode I) and shear sliding (mode II) along grain boundaries.

- The interfacial property of grain boundaries has remarkable effect on the bulk failure load of the microcantilever beam, which increases with both the cohesive strength and the total fracture energy of the grain boundary.

Acknowledgements

References

[1] P. Badica, H. Borodianska, S.M. Xie, T. Zhao, D. Demirskyi, P.F. Li, A.I.Y. Tok, Y. Sakka, O. Vasylkiv, Toughness control of boron carbide obtained by spark plasma sintering in nitrogen atmosphere, Ceram. Int. 40(2) (2014) 3053-3061.

[2] P. Badica, S. Grasso, H. Borodianska, S.S. Xie, P.F. Li, P. Tatarko, M.J. Reece, Y. Sakka, O. Vasylkiv, Tough and dense boron carbide obtained by high-pressure (300 MPa) and low-temperature (1600 degrees C) spark plasma sintering, J. Ceram. Soc. Jpn. 122(1424) (2014) 271-275.

[3] R.H. Kraft, J.F. Molinari, A statistical investigation of the effects of grain boundary properties on transgranular fracture, Acta Mater. 56(17) (2008) 4739-4749.

[4] S.M.T. Mousavi, N. Richart, C. Wolff, J.F. Molinari, Dynamic crack propagation in a heterogeneous ceramic microstructure, insights from a cohesive model, Acta Mater. 88 (2015) 136-146.

[5] J.D. Clayton, R.H. Kraft, R.B. Leavy, Mesoscale modeling of nonlinear elasticity and fracture in ceramic polycrystals under dynamic shear and compression, Int. J. Solids Struct. 49(18) (2012) 2686-2702.

[6] S.R. Witek, G.A. Miller, M.P. Harmer, Effects of CaO on the strength and toughness of AlN, J. Am. Ceram. Soc. 72(3) (1989) 469-473.

[7] C.J. Shih, M.A. Meyers, V.F. Nesterenko, S.J. Chen, Damage evolution in dynamic deformation of silicon carbide, Acta Mater. 48(9) (2000) 2399-2420.

[8] J.M. Staehler, W.W. Predebon, B.J. Pletka, G. Subhash, Strain-rate effects in high-purity alumina, JOM-J. Miner. Met. Mater. Soc. 47(5) (1995) 60-63.

[9] Z. Wang, P. Li, Dynamic failure and fracture mechanism in alumina ceramics: Experimental observations and finite element modelling, Ceram. Int. 41(10, Part A) (2015) 12763-12772.

[10] Z. Wang, P. Li, Characterisation of dynamic behaviour of alumina ceramics: evaluation of stress uniformity, AIP Adv. 5(10) (2015) 107224.

[11] S. Acharya, S. Bysakh, V. Parameswaran, A.K. Mukhopadhyay, Deformation and failure of alumina under high strain rate compressive loading, Ceram. Int. 41(5) (2015) 6793-6801.

[12] O. Johari, N.M. Parikh, Scanning electron fractographic study of aluminum oxide as a function of testing temperature and grain size, Fracture Mechanics of Ceramics. Concepts, Flaws, and Fractography1974, pp. 399-420.

[13] R.M. Spriggs, J.B. Mitchell, T. Vasilos, Mechanical properties of pure, dense aluminum oxide as a function of temperature and grain size, J. Am. Ceram. Soc. 47(7) (1964) 323-327.

[14] A.C. Lewis, J.F. Bingert, D.J. Rowenhorst, A. Gupta, A.B. Geltmacher, G. Spanos, Two- and three-dimensional microstructural characterization of a super-austenitic stainless steel, Mater. Sci. Eng. A 418(1-2) (2006) 11-18.

[15] M. Nygards, P. Gudmundson, Three-dimensional periodic Voronoi grain models and micromechanical FE-simulations of a two-phase steel, Comput. Mater. Sci. 24(4) (2002) 513-519.

[16] M. Ohata, M. Suzuki, A. Ui, F. Minami, 3D-Simulation of ductile failure in two-phase structural steel with heterogeneous microstructure, Eng. Fract. Mech. 77(2) (2010) 277-284.

[17] J. Li, H. Proudhon, A. Roos, V. Chiaruttini, S. Forest, Crystal plasticity finite element simulation of crack growth in single crystals, Comput. Mater. Sci. 94 (2014) 191-197.

[18] S. Falco, P. Siegkas, E. Barbieri, N. Petrinic, A new method for the generation of arbitrarily shaped 3D random polycrystalline domains, Comput. Mech. 54(6) (2014) 1447-1460.

[19] S.I. Ranganathan, M. Ostoja-Starzewski, Scaling function, anisotropy and the size of RVE in elastic random polycrystals, J. Mech. Phys. Solids 56(9) (2008) 2773-2791.

[20] X.W. Zhou, J.A. Zimmerman, E.D. Reedy, N.R. Moody, Molecular dynamics simulation based cohesive surface representation of mixed mode fracture, Mech. Mater. 40(10) (2008) 832-845.

[21] Z.N. Zhang, X.R. Ge, A new quasi-continuum constitutive model for crack growth in an isotropic solid, Eur. J. Mech. A-Solid 24(2) (2005) 243-252.

[22] T.T. Zhou, C.Z. Huang, Simulation of crack propagation in single phase ceramic tool materials, Comput. Mater. Sci. 104 (2015) 177-184.

[23] M.A. Groeber, B.K. Haley, M.D. Uchic, D.M. Dimiduk, S. Ghosh, 3D reconstruction and characterization of polycrystalline microstructures using a FIB-SEM system, Mater. Charact. 57(4-5) (2006) 259-273.

[24] M.D. Uchic, M.A. Groeber, D.M. Dimiduk, J.P. Simmons, 3D microstructural characterization of nickel superalloys via serial-sectioning using a dual beam FIB-SEM, Scr. Mater. 55(1) (2006) 23-28.

[25] S.F. Nielsen, E.M. Lauridsen, D.J. Jensen, H.F. Poulsen, A three-dimensional X-ray diffraction microscope for deformation studies of polycrystals, Mater. Sci. Eng. A 319 (2001) 179-181.

[26] Z. Zhao, S. Kuchnicki, R. Radovitzky, A. Cultino, Influence of in-grain mesh resolution on the prediction of deformation textures in fcc polycrystals by crystal plasticity FEM, Acta Mater. 55(7) (2007) 2361-2373.

[27] F. Aurenhammer, Voronoi diagrams - a survey of a fundamental geometric data structure, Comput. Surv. 23(3) (1991) 345-405.

[28] I. Benedetti, M.H. Aliabadi, A three-dimensional grain boundary formulation for microstructural modeling of polycrystalline materials, Comput. Mater. Sci. 67 (2013) 249-260.

[29] F. Wakai, N. Enomoto, H. Ogawa, Three-dimensional microstructural evolution in ideal grain growth - General statistics, Acta Mater. 48(6) (2000) 1297-1311.

[30] A. Rinaldi, D. Krajcinovic, P. Peralta, Y.C. Lai, Lattice models of polycrystalline micro structures: A quantitative approach, Mech. Mater. 40(1-2) (2008) 17-36.

[31] H. Ritz, P.R. Dawson, Sensitivity to grain discretization of the simulated crystal stress distributions in FCC polycrystals, Model. Simul. Mater. Sci. Eng. 17(1) (2009) 015001.

[32] R. Morrell, Handbook of Properties of Technical & Engineering Ceramics: Part 2: Data Reviews: Section 1: High-Alumina Ceramics, Her Majesty's Stationery Office, London, 1987.

[33] R.M. Spriggs, L.A. Brissette, Expressions for shear modulus and Poisson's ratio of porous refractory oxides, J. Am. Ceram. Soc. 45(4) (1962) 198-199.

[34] R. Quey, P.R. Dawson, F. Barbe, Large-scale 3D random polycrystals for the finite element method: Generation, meshing and remeshing, Comput. Method. Appl. M. 200(17-20) (2011) 1729-1745.

[35] C. Geuzaine, J.F. Remacle, Gmsh: A 3-D finite element mesh generator with built-in pre- and post-processing facilities, Int. J. Numer. Methods Eng. 79(11) (2009) 1309-1331.

[36] T. Vodenitcharova, L.C. Zhang, I. Zarudi, Y. Yin, H. Domyo, T. Ho, M. Sato, The effect of anisotropy on the deformation and fracture of sapphire wafers subjected to thermal shocks, J. Mater. Proc. Technol. 194(1-3) (2007) 52-62.

[37] J.M. Winey, Y.M. Gupta, D.E. Hare, r-axis sound speed and elastic properties of sapphire single crystals, J. Appl. Phys. 90(6) (2001) 3109-3111.

[38] J.R. Gladden, J.H. So, J.D. Maynard, P.W. Saxe, Y. Le Page, Reconciliation of ab initio theory and experimental elastic properties of Al_2O_3, Appl. Phys. Lett. 85(3) (2004) 392-394.

[39] D.B. Hovis, A. Reddy, A.H. Heuer, X-ray elastic constants for alpha-Al_2O_3, Appl. Phys. Lett. 88(13) (2006) 131910.

[40] K.L. Nielsen, J.W. Hutchinson, Cohesive traction-separation laws for tearing of ductile metal plates, Int. J. Impact Eng. 48 (2012) 15-23.

[41] K. Park, G.H. Paulino, Cohesive zone models: A critical review of traction-separation relationships across fracture surfaces, Appl. Mech. Rev. 64(6) (2011) 060802.

[42] T. Diehl, On using a penalty-based cohesive-zone finite element approach, Part I: Elastic solution benchmarks, Int. J. Adhes. Adhes. 28(4-5) (2008) 237-255.

List of Tables

Table 1   Anisotropic elastic constants of polycrystalline alumina [39].

| Parameter	C_{11}	C_{12}	C_{13}	C_{14}	C_{33}	C_{44}
Value (GPa)	497	163	116	22	501	147

List of Figures

Fig. 1   Microstructure of an alumina specimen which was thermally etched.
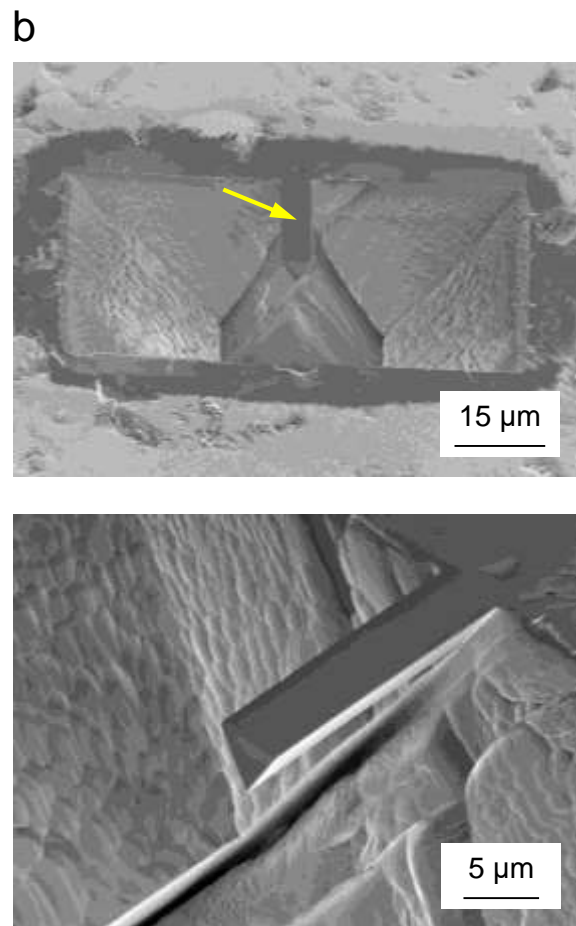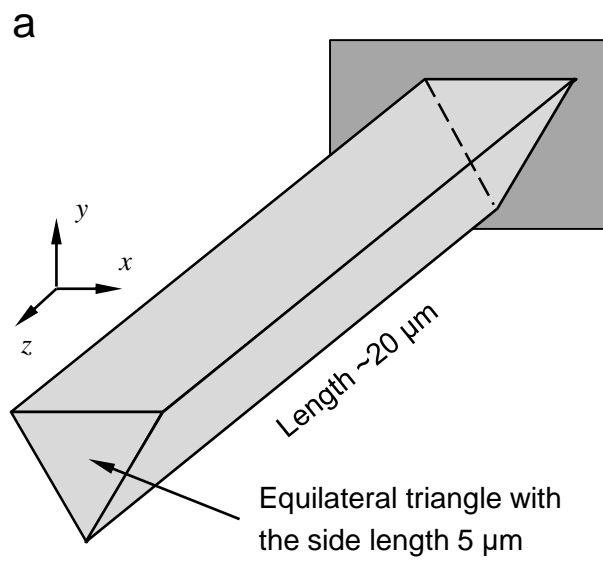
Fig. 2   (a) The schematic of a microcantilever beam for bending experiments, and (b) a typical alumina microcantilever specimen prepared by focused ion beam technique.

Fig. 3   (a) The measured load history applied at the free end of an alumina microcantilever beam, and (b) the load versus displacement curve. Note that given the initial indentation into the specimen surface, the measured displacement of the nanoindenter tip is corrected to calculate the deflection of the microcantilever beam at the free end.

Fig. 4   Typical fracture feature of two alumina microcantilever beams subjected to bending loads. Both the beams failed near the fixed end.

Fig. 5   The finite element model of an alumina microcantilever beam for bending tests: (a) the polycrystalline geometry generated by hardcore Voronoi tessellation, (b) the FE meshes, and (c) the cohesive elements for grain boundaries.

Fig. 6   The traction–separation relation to characterise the damage initiation (point a) and evolution (line ab) of cohesive layers for grain boundaries.

Fig. 7   The cubic representative elementary volume of polycrystalline alumina with the different number of grains: (a) 30, (b) 60 and (c) 90.

Fig. 8   Effect of the number of grains on Young's modulus of the cubic REV alumina. The average modulus for each grain number is calculated from

the predictions for the combination of 10 crystalline morphologies and 10 grain orientations. Note that the Young's modulus is typically 398–400 GPa for engineering alumina with the purity 99.5% and the porosity <1% [32, 33].

Fig. 9   Comparison between the FE predicted and experimentally measured load versus displacement curves at the free end of an alumina microcantilever beam subjected to bending loads. Note that the FE simulation was rerun on the beam in which the grains were assigned with six sets of random grain orientations.

Fig. 10   Predicted longitudinal stress distribution in the alumina microcantilever beam at the elastic stage (approximately at the displacement 200 nm in Fig. 9) during a bending load. The figures (a) and (b) compare the predictions using two different grain orientations in the model.

Fig. 11   Predicted longitudinal stress distribution in the alumina microcantilever beam at five different stages during a bending load. The five stages (a–e) are indicated in the predicted load versus displacement curve (one of the predicted curves in Fig. 9).

Fig. 12   Predicted maximum principal stress distribution in the grain boundaries (cohesive elements) in the alumina microcantilever beam at five different stages during a bending load. The five stages (a–e) are indicated in the predicted load versus displacement curve (one of the predicted curves in Fig. 9).

Fig. 13   Shear sliding and tensile opening along grain boundaries near the fixed end of the polycrystalline alumina microcantilever beam: (a) the FE prediction at the final stage of the fracture process (refer to Fig. 11(e)), and (b) the schematic during the fracture process.

Fig. 14   Predicted load versus displacement curves of an alumina microcantilever beam as a function of the cohesive strength (T_0) and the damage initiation ratio (δ_0/δ_f) of cohesive layers which are defined for grain boundaries.
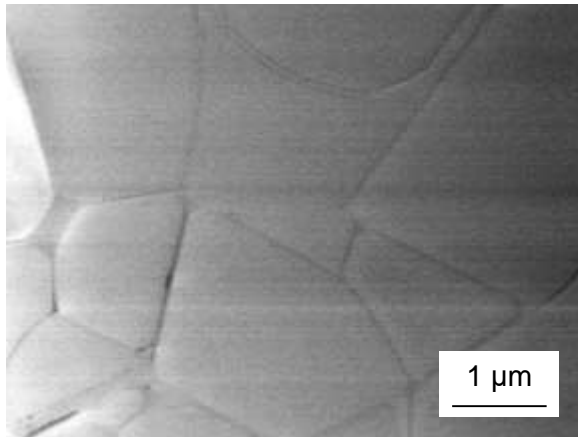
Figure 1: Microstructure of an alumina specimen which was thermally etched.

Figure 2: (a) The schematic of a microcantilever beam for bending experiments, and (b) a typical alumina microcantilever specimen prepared by focused ion beam technique.
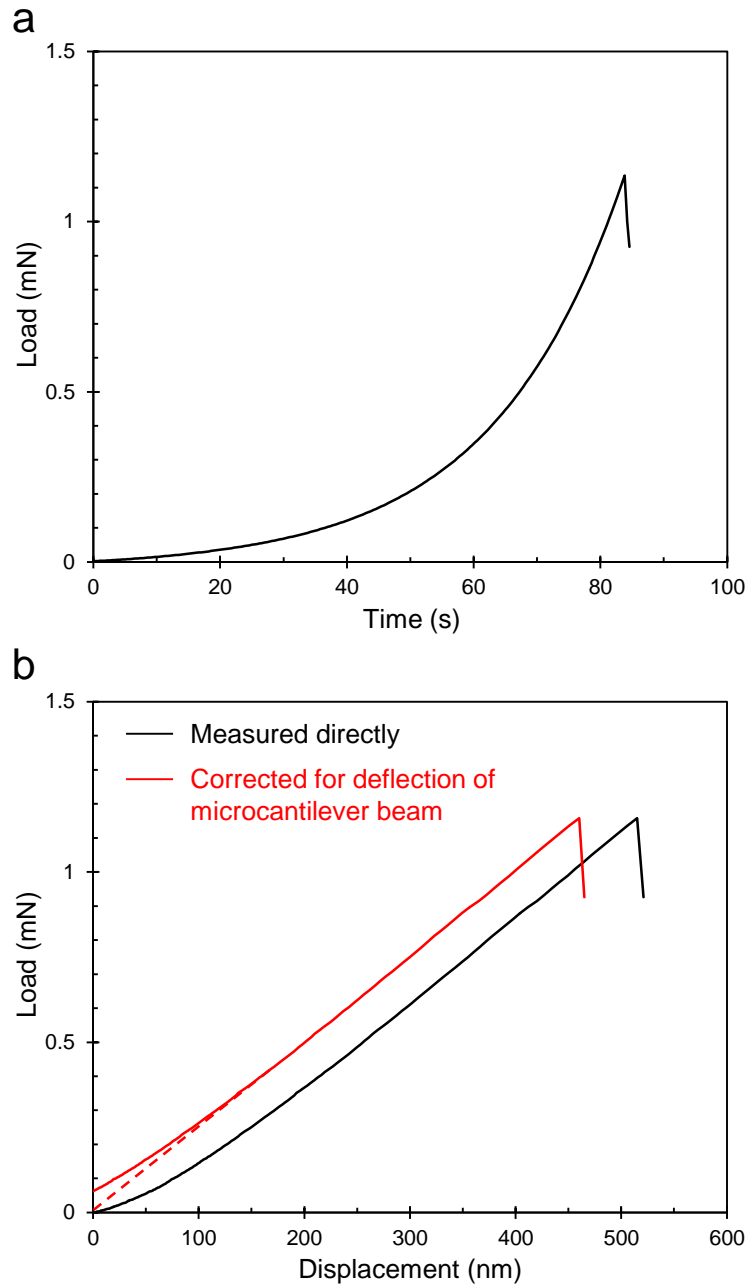
Figure 3: (a) The measured load history applied at the free end of an alumina microcantilever beam, and (b) the load versus displacement curve. Note that given the initial indentation into the specimen surface, the measured displacement of the nanoindenter tip is corrected to calculate the deflection of the microcantilever beam at the free end.
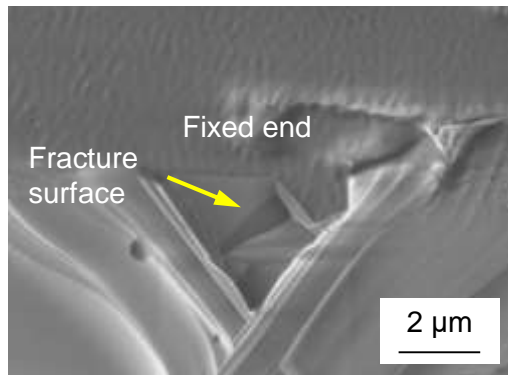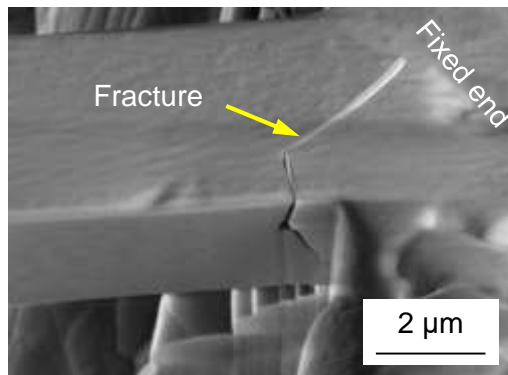
Figure 4: Typical fracture feature of two alumina microcantilever beams subjected to bending loads. Both the beams failed near the fixed end.

a

Fixed end

Loading tip

b

c
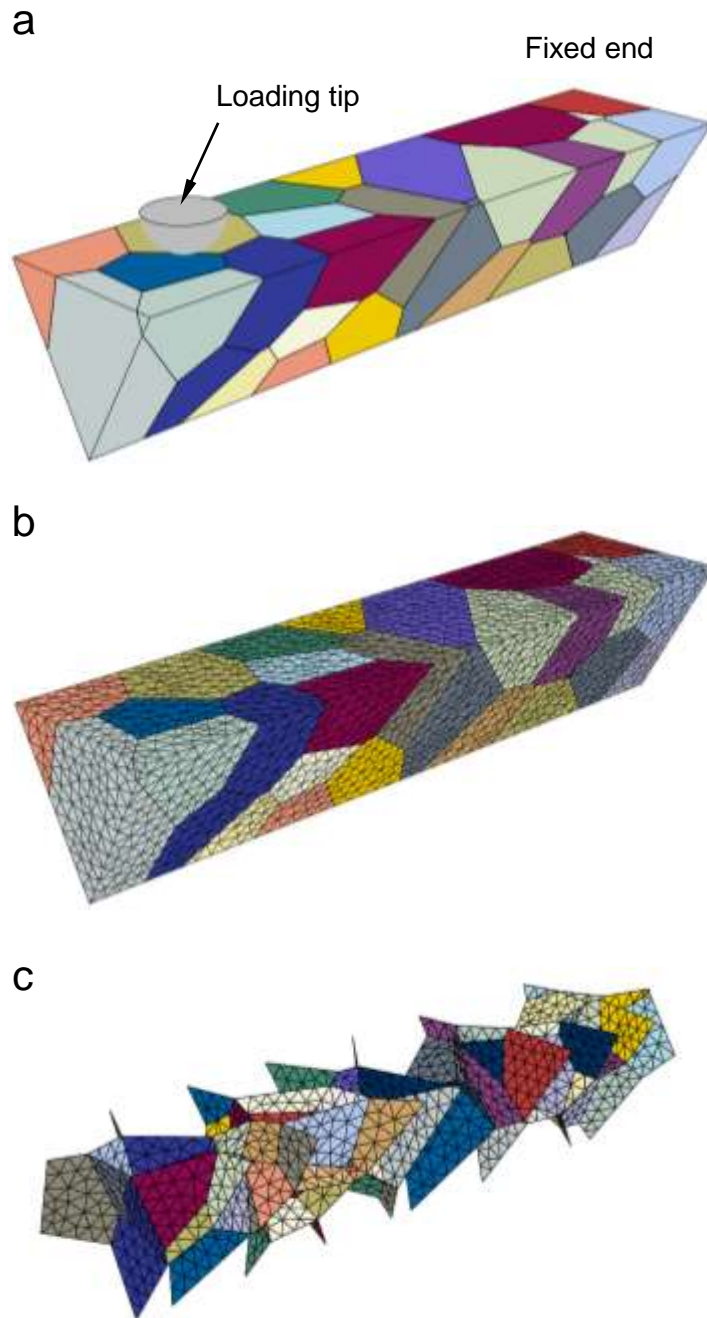
Figure 5: The finite element model of an alumina microcantilever beam for bending tests: (a) the polycrystalline geometry generated by hardcore Voronoi tessellation, (b) the FE meshes, and (c) the cohesive elements for grain boundaries.
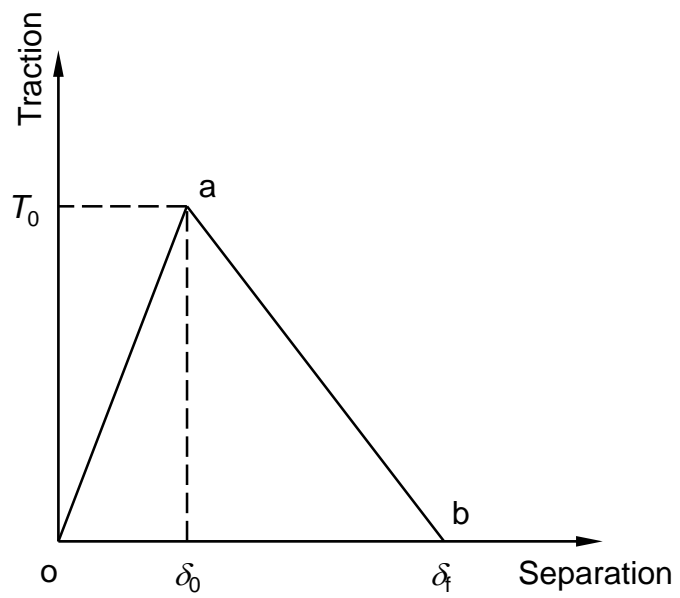
Figure 6: The traction–separation relation to characterise the damage initiation (point a) and evolution (line ab) of cohesive layers for grain boundaries.
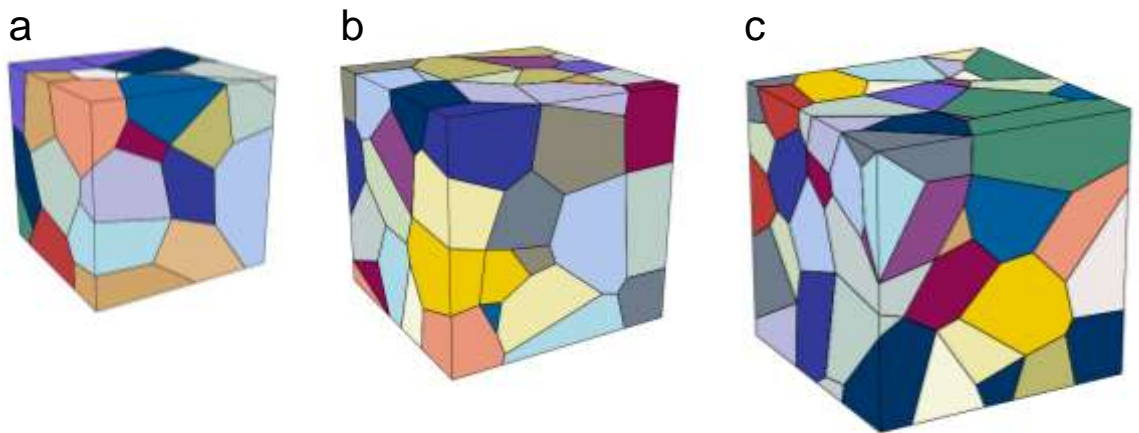
Figure 7: The cubic representative elementary volume of polycrystalline alumina
with the different number of grains: (a) 30, (b) 60 and (c) 90.
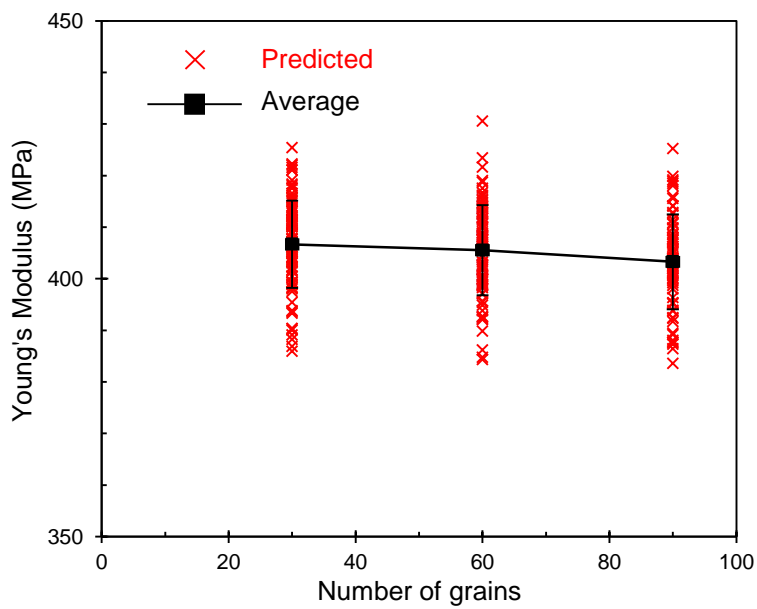
Figure 8: Effect of the number of grains on Young's modulus of the cubic REV alumina. The average modulus for each grain number is calculated from the predictions for the combination of 10 crystalline morphologies and 10 grain orientations. Note that the Young's modulus is typically 398–400 GPa for engineering alumina with the purity 99.5% and the porosity <1% [32, 33].
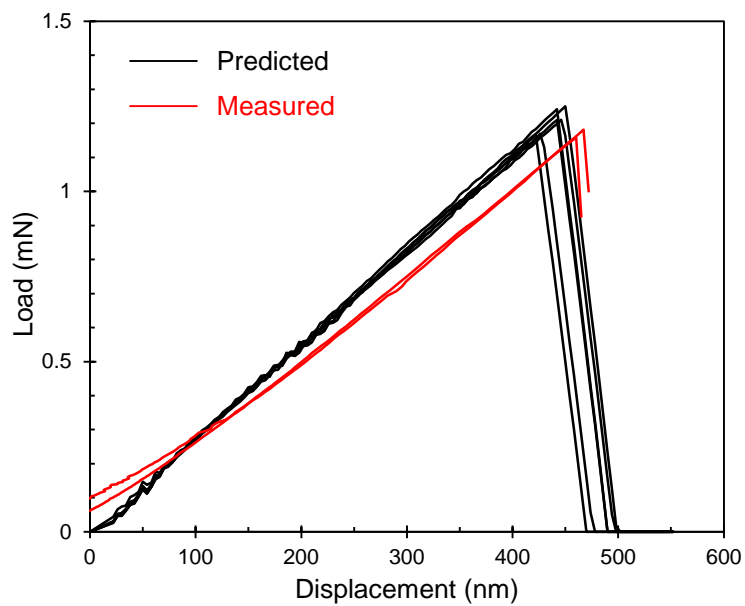
Figure 9: Comparison between the FE predicted and experimentally measured load versus displacement curves at the free end of an alumina microcantilever beam subjected to bending loads. Note that the FE simulation was rerun on the beam in which the grains were assigned with six sets of random grain orientations.
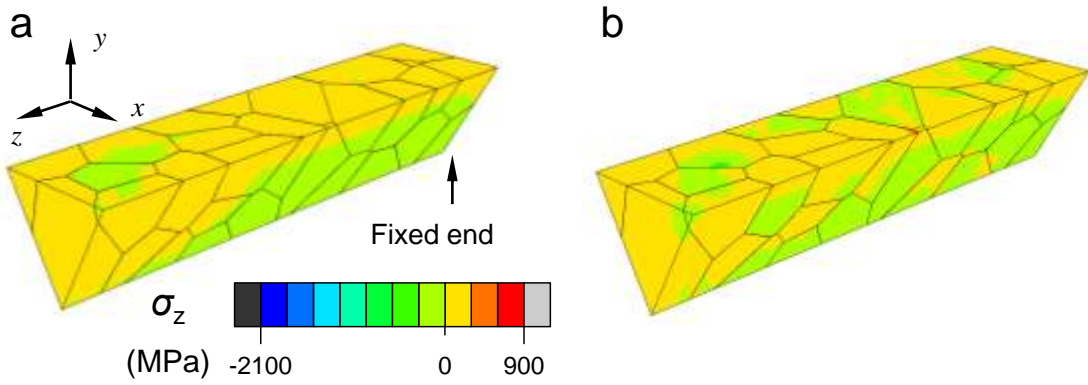
Figure 10: Predicted longitudinal stress distribution in the alumina microcantilever beam at the elastic stage (approximately at the displacement 200 nm in Fig. 9) during a bending load. The figures (a) and (b) compare the predictions using two different grain orientations in the model.
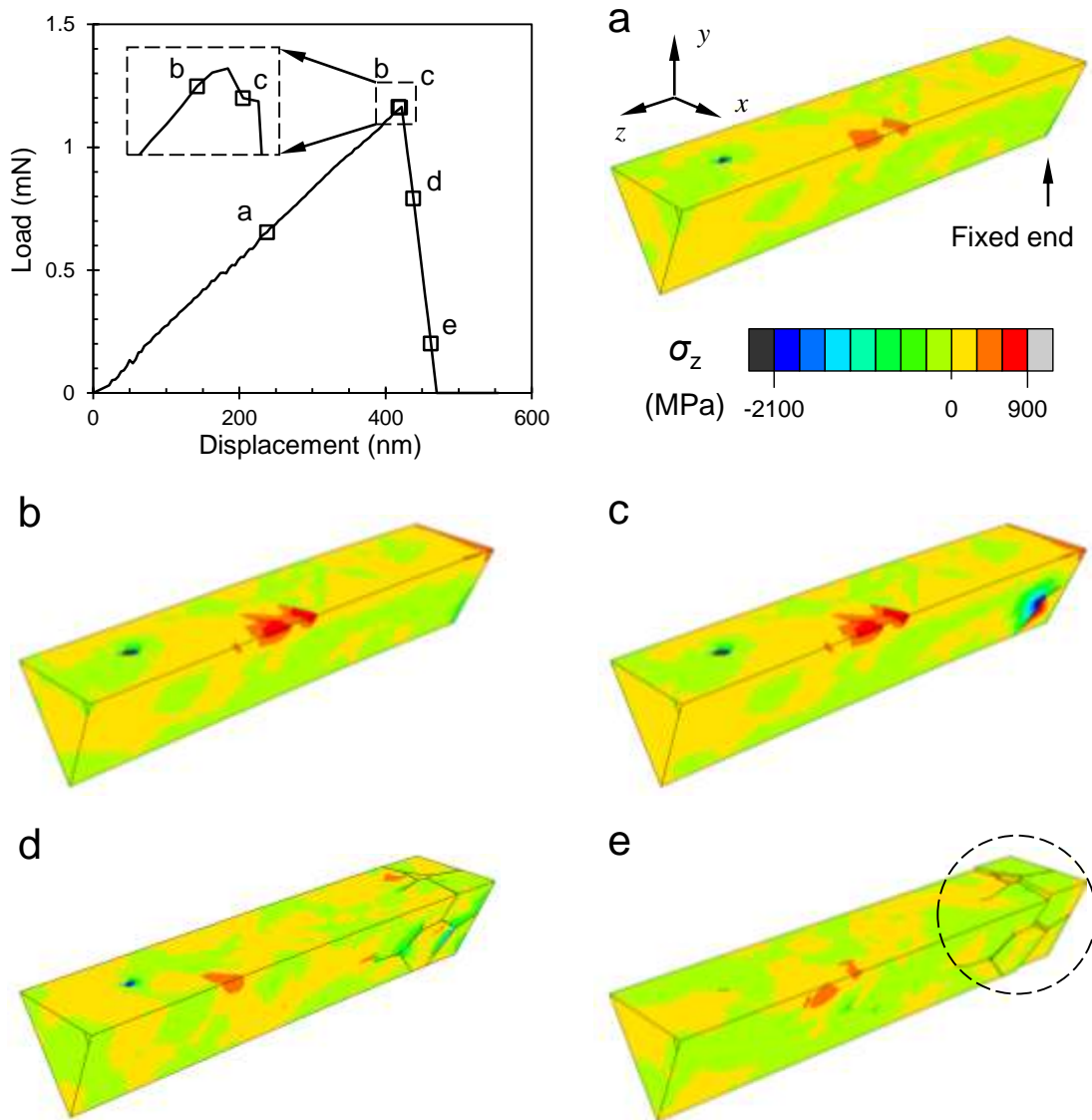
Figure 11: Predicted longitudinal stress distribution in the alumina microcantilever beam at five different stages during a bending load. The five stages (a–e) are indicated in the predicted load versus displacement curve (one of the predicted curves in Fig. 9).
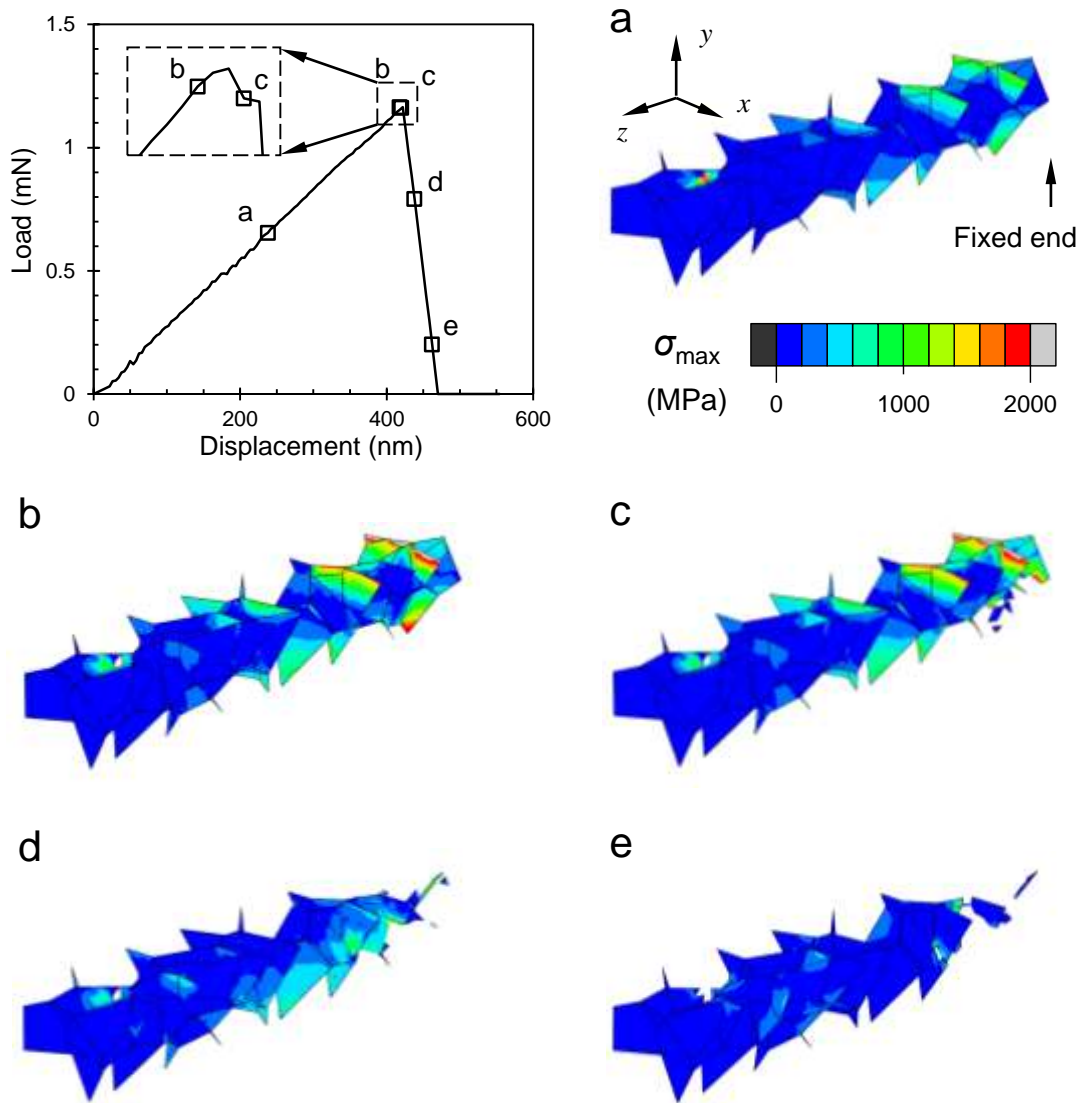
Figure 12: Predicted maximum principal stress distribution in the grain boundaries (cohesive elements) in the alumina microcantilever beam at five different stages during a bending load. The five stages (a–e) are indicated in the predicted load versus displacement curve (one of the predicted curves in Fig. 9).
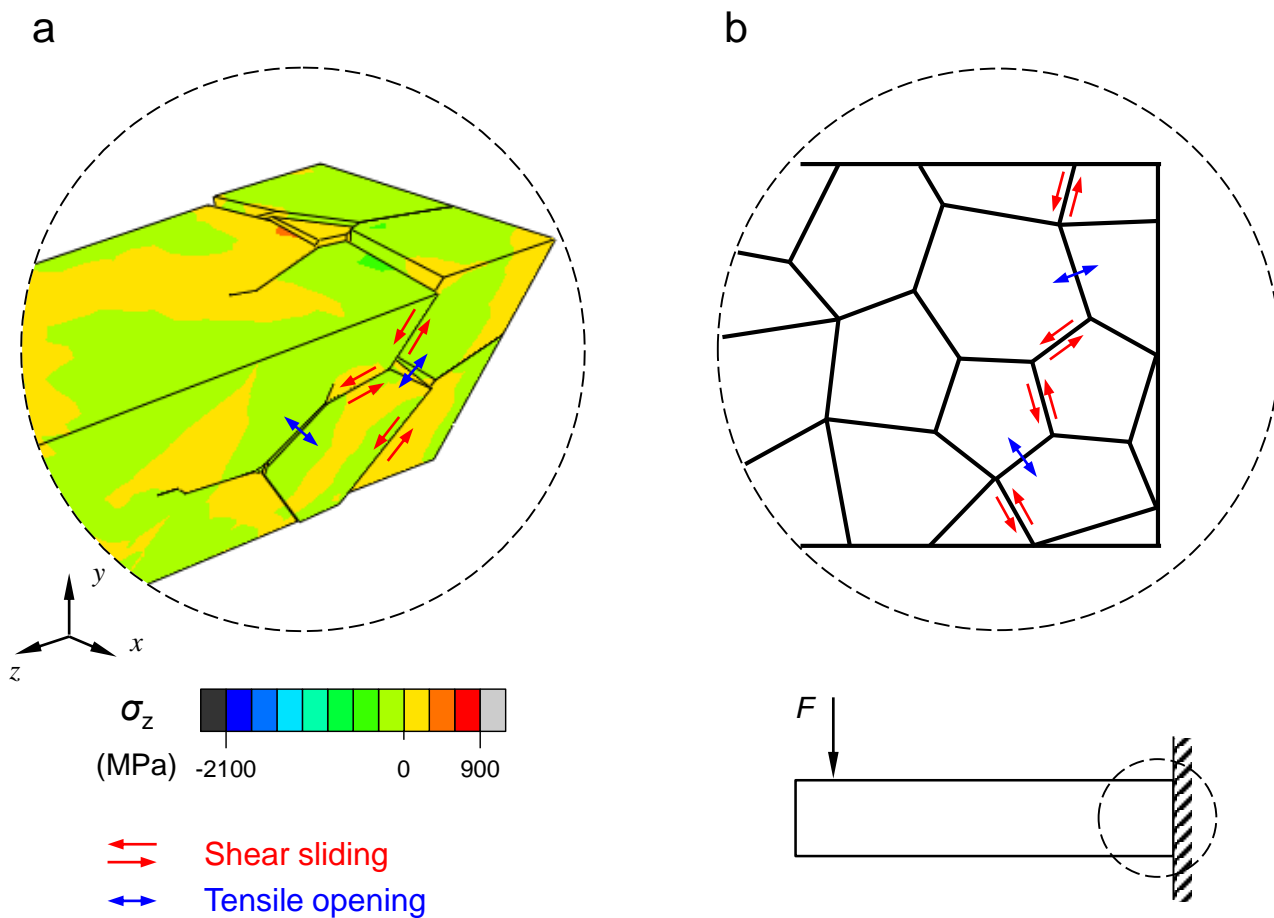
Figure 13: Shear sliding and tensile opening along grain boundaries near the fixed end of the polycrystalline alumina microcantilever beam: (a) the FE prediction at the final stage of the fracture process (refer to Fig. 11(e)), and (b) the schematic during the fracture process.
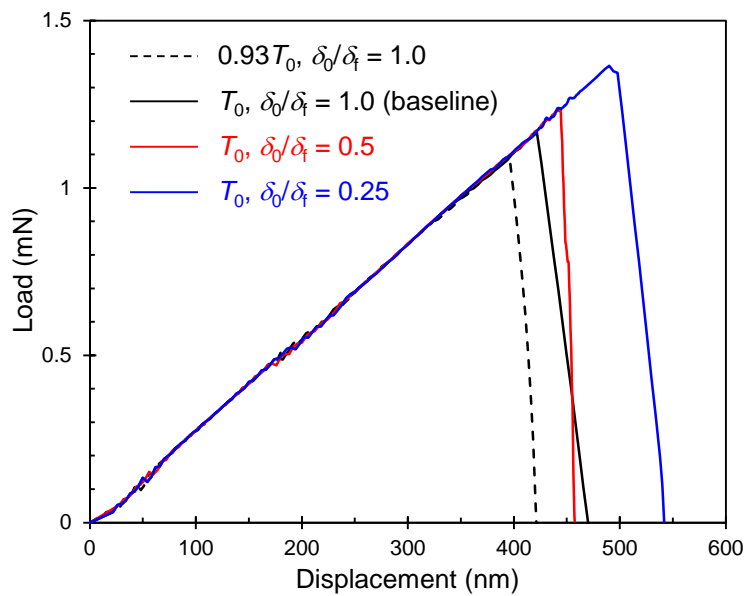
Figure 14: Predicted load versus displacement curves of an alumina microcantilever beam as a function of the cohesive strength (T_0) and the damage initiation ratio (δ_0/δ_f) of cohesive layers which are defined for grain boundaries.